Resolving macro- and micro-porous layer interaction in polymer electrolyte fuel cells using focused ion beam and X-ray computed tomography

E.A. Wargo [a], V.P. Schulz [c], A. Çeçen [a,b], S.R. Kalidindi [b], E.C. Kumbur [a,*]

[a] Electrochemical Energy Systems Laboratory, Department of Mechanical Engineering and Mechanics, Drexel University, Philadelphia, PA 19104, USA
[b] Mechanics of Microstructures Group, Department of Mechanical Engineering and Mechanics, Drexel University, Philadelphia, PA 19104, USA
[c] Baden-Wuerttemberg Cooperative State University, Mannheim, Germany

ARTICLE INFO

ABSTRACT

In this study, the microstructure of a dual-layer polymer electrolyte fuel cell diffusion media (DM) sample is characterized using micro X-ray computed tomography and focused ion beam-scanning electron microscopy to determine the contributions of the gas diffusion layer (GDL) and the micro-porous layer (MPL) regions on the overall transport characteristics of the DM. The measured 3-D data is processed to extract the microstructure datasets of the MPL-only region, GDL-only region, and GDL–MPL assembly. These datasets are then analyzed using in-house microstructure analysis tools and a full pore morphology model to determine the water imbibition characteristics and the key structure-related transport properties, including the phase volume fractions, pore connectivity, tortuosity, diffusivity coefficient, pore size distribution, permeability, and capillary pressure–saturation curves. Results indicate that the structure of the MPL has a significant impact on the transport properties of the GDL–MPL assembly. When the GDL-only dataset is compared with the GDL–MPL assembly, the addition of the MPL is found to cause an increase in tortuosity of ~10%, and a decrease of nearly 50% in the structural diffusivity coefficient of the overall GDL–MPL assembly. Furthermore, notable differences are observed in the water imbibition characteristics of the GDL and the MPL due to the differences in microstructure of these regions.

1. Introduction

Polymer electrolyte fuel cells (PEFCs) hold great promise as an alternative power source for use in a wide range of applications. Current research efforts on PEFCs are focused on improving the performance and durability of these systems, both of which are inherently governed by the materials used in these systems [1,2]. The complex internal structure (henceforth referred to as "microstructure") of these materials ultimately defines their characteristic transport properties and ability to manage water within the PEFC. Among the PEFC components, significant effort has been placed on understanding the role of the porous diffusion media (DM), which has been shown to be a vital component for maintaining effective water management during PEFC operation [1–13].

In a PEFC, the porous DM serves to provide a uniform distribution of the reactants in the electrodes, while allowing for the transport of product water and electrons [5]. The DM typically consists of an electrically conductive macro-substrate (i.e., macro-DM, also referred to as the gas diffusion layer, or GDL) coated with a micro-porous layer (MPL). Both regions (i.e., GDL and MPL) greatly influence the multiphase transport characteristics of the DM, affecting the distribution of water inside the PEFC. Many studies [6–13] indicate that the proper engineering of DM materials may lead to an optimized water balance inside the cell. However, the proper selection of DM materials with desired internal architecture is currently hindered by a lack of understanding of how the structure of this component governs the multiphase flow in PEFCs.

Numerous studies have been performed to investigate the transport characteristics of the DM [6–13]. Due to the complex structure of the DM, the field is mostly saturated by studies that focus on quantifying the bulk transport behavior of the DM. In these studies, the basic morphological features of the DM (e.g., porosity, permeability, pore size distribution) have been investigated to correlate the internal structure of the DM to PEFC performance [6,8,10,14–16]. While a good deal of understanding regarding the bulk properties of the DM has been achieved through these experimental studies, the composite nature of the DM makes it difficult to experimentally determine the impact of the GDL and MPL substrates on the overall DM due to the indistinct interface between these regions [17]. As a result, the investigation of macro- and micro-porous layer interaction in DM has been limited to mostly modeling studies.

Numerous mathematical models have been developed to investigate the transport characteristics of the GDL and MPL substrates.

---

* Corresponding author. Tel.: +1 215 895 5871; fax: +1 215 895 1478.
  E-mail address: kumbur@drexel.edu (E.C. Kumbur).

An extensive review of the recent modeling efforts is provided in Ref. [12]. Among the modeling approaches, macroscopic models are considered to be quite powerful tools for quantifying the impact of the effective transport properties of these regions on PEFC performance. However, one major issue with these modeling efforts is that in these models, the GDL and MPL are treated as homogeneous materials, and transport phenomena therein is presumed to be described by correlations developed for idealized materials [18–22]. In addition, in these models, the MPL and GDL regions are typically treated as separate adjacent layers with a sharp interface [12]; however, in reality the MPL is prepared as a slurry coated on the GDL substrate [5,11], resulting in a composite GDL–MPL assembly with *no distinct interface*. The existence of a non-distinct interface between the GDL and MPL has also been experimentally demonstrated in recent studies by Swamy et al. [3], Fishman and Bazylak [17], and Preston et al. [23].

Pore-scale modeling approaches have the ability to overcome some of the major limitations of macroscopic models, as they allow for the examination of physical phenomena at different length scales within the materials of interest. Several approaches have been adopted in PEFC studies, including the pore network modeling (PNM) approach [24–26], lattice-Boltzmann (LB) method [27–29], and volume of fluid (VOF) method [30,31]. Among the pore-scale analysis tools, PNM has become quite popular due to its computational efficiency. In PNM, the structure of interest can be represented as a simplified arrangement of pores, throats, and solid to mimic the water transport in the GDL and MPL regions. Several studies have also utilized high-resolution 3-D imaging techniques such as X-ray computed tomography (XCT) and focused ion beam–scanning electron microscopy (FIB–SEM) to measure the microstructure of fuel cell DM and use the measured structure as a computational domain in pore-scale modeling studies [28,29,32]. One major issue with these models is that they are fairly computationally intensive; therefore, these models are limited to analyzing very small volumes, which may not be sufficient to capture the overall structure of the GDL and MPL and draw meaningful conclusions regarding the role of these regions on the overall GDL–MPL assembly. The large variation in length scales between the GDL and MPL regions, and the indistinct GDL|MPL interface necessitate a more complicated modeling domain which is computationally expensive and difficult to be handled by pore-scale models.

The objective of this study is to combine recent advances in 3-D microstructure quantification and pore-scale transport analysis to assess the contribution of the GDL and MPL regions on the overall transport characteristics of the DM. As such, the microstructure of a dual-layer DM sample was characterized using XCT and FIB–SEM. Based on these measurements, three datasets, namely the MPL-only, GDL-only, and GDL–MPL assembly, were obtained and examined using a suite of microstructure analysis tools and a pore-scale transport model to determine the water imbibition characteristics and the key structure-related transport properties, including: the phase volume fractions, pore connectivity, tortuosity, pore size distribution, diffusivity coefficient, permeability, and capillary pressure–saturation curves. A detailed analysis of the measured structural features of these regions along with their transport properties was performed, and the contribution of each region on the overall transport behavior of the GDL–MPL assembly was illuminated.

2. Method of approach

In this study, a SIGRACET® SGL 10BC sample was selected to analyze the three regions of interest, namely: MPL-only region, GDL-only region, and overall GDL–MPL assembly. The method used to evaluate the key structure-related properties of these

regions consists of three main steps: (i) microstructure dataset acquisition and image processing, which was conducted separately for the MPL region, GDL region, and overall GDL–MPL assembly; (ii) structure and transport property analyses of the microstructure datasets using in-house microstructure analysis tools and a full pore morphology model; and (iii) combined analysis of the GDL–MPL assembly. Each step is described in detail below, and a flow chart outlining the main steps of our approach is shown in Fig. 1.

2.1. Dataset acquisition and image processing

2.1.1. MPL microstructure acquisition via FIB–SEM
As a first step, an FEI Strata[TM] DB 235 FIB–SEM [29,33] was used to perform nanotomography on the MPL region of the DM sample [34,35] due to the small pore size of the MPL. An MPL volume of $\sim$5 μm × 8 μm × 2 μm was captured by serial sectioning of 150 slices with an image resolution of $\sim$10 nm and a slice thickness of 20 nm. A 1.5 μm layer of platinum was deposited over the volume of interest prior to serial sectioning to prevent ion damage, and the volume of interest was exposed as a peninsula to reduce shadows in the captured images. During image acquisition, the images of the stack may be misaligned due to beam shift and/or sample drift. Such misalignments were corrected by applying a discrete Fourier transform registration code on the images. To correct for the projection effects (which result from imaging with the SEM source angled at 52°), each image was stretched vertically and shifted downward.

Once the images were corrected, several thresholding techniques were tested to segment the captured SEM images into pore and material phases. Among the segmentation techniques tested, the iterative ISODATA method [36–38] was observed to produce the best segmentation upon visual inspection (Fig. 2a) and resulted in a porosity value which is in good agreement with literature [29,39,40]. Following segmentation, the images were stacked in 3-D and further analyzed to remove any material islands that appear to be floating in space. An example of the final 3-D reconstruction of the MPL sample is shown in Fig. 3(bottom). More detailed information regarding the MPL dataset acquisition and image processing can be found in our previous publications [34,35].

2.1.2. Capturing GDL–MPL assembly via XCT
A SkyScan 1172 high-resolution XCT was employed at a source voltage of 37 kV and a step size of 0.1° to capture the 3-D microstructure of the GDL–MPL assembly. The XCT dataset contains three primary phases of interest: void, MPL, and solid fiber, which are listed in order of increasing density and show up in the reconstructed images as black, gray, and white, respectively (see Fig. 2b). Consequently, many of the thresholding methods used previously to segment the FIB–SEM dataset cannot be applied to the GDL–MPL assembly, because they are binary methods and can only separate images into two phases. Here, we used a fully automated multi-phase method developed by Simmons et al. [41] to segment the XCT data. This method is based on the maximization of posterior marginals (MPM), which allows for consideration of both the grayscale value of pixels as well as the classification (phase) of neighboring pixels [41]. This segmentation scheme also incorporates an expectation maximization algorithm with simulated annealing (referred to as EM/MPM/SA) [41]. Expectation maximization (EM) optimizes the Gaussian fits of the grayscale data used in the MPM method. The simulated annealing (SA) component of the algorithm imposes a cost for having neighboring pixels of a different class. This cost is increased as EM/MPM cycles are executed, which helps to decrease noise in the data by sharpening the interfaces between phases.

Following segmentation, the dataset was further analyzed in 3-D to remove any islands of MPL and/or fiber phase that appear to be
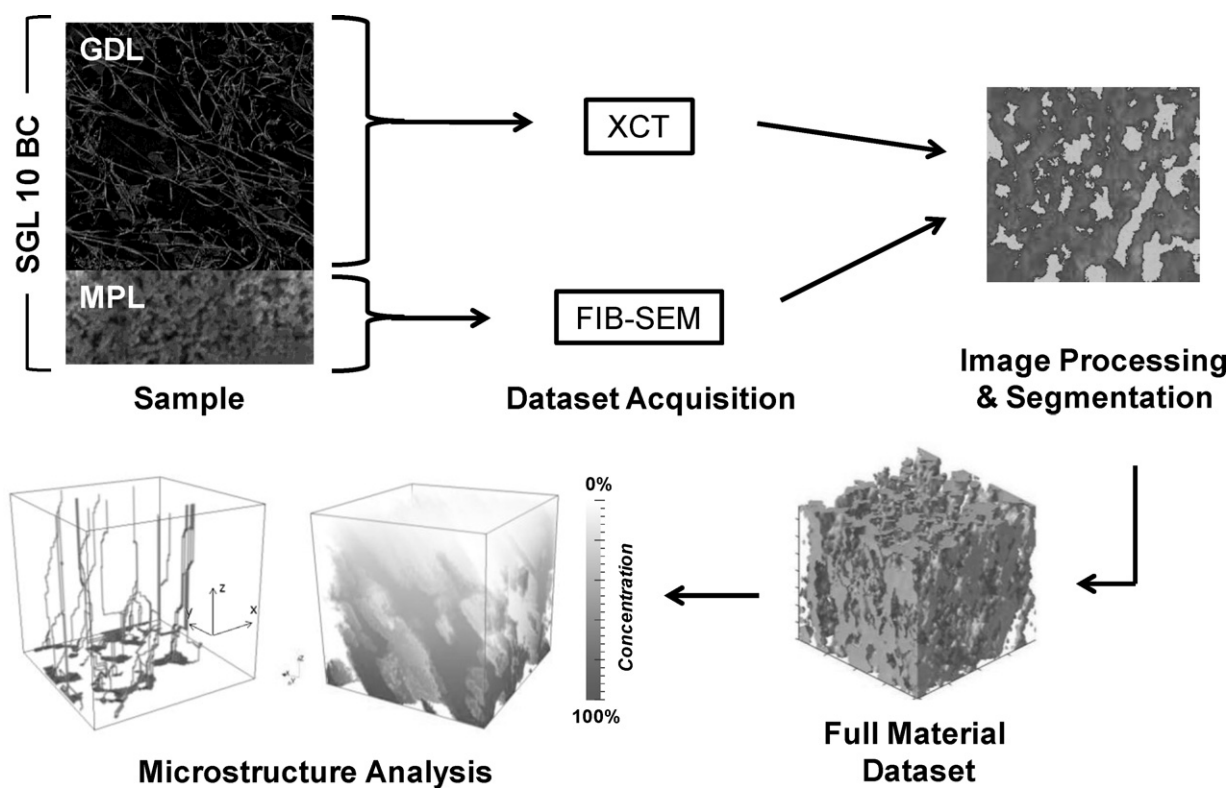
Fig. 1. Flow chart outlining the method of approach of the present study.
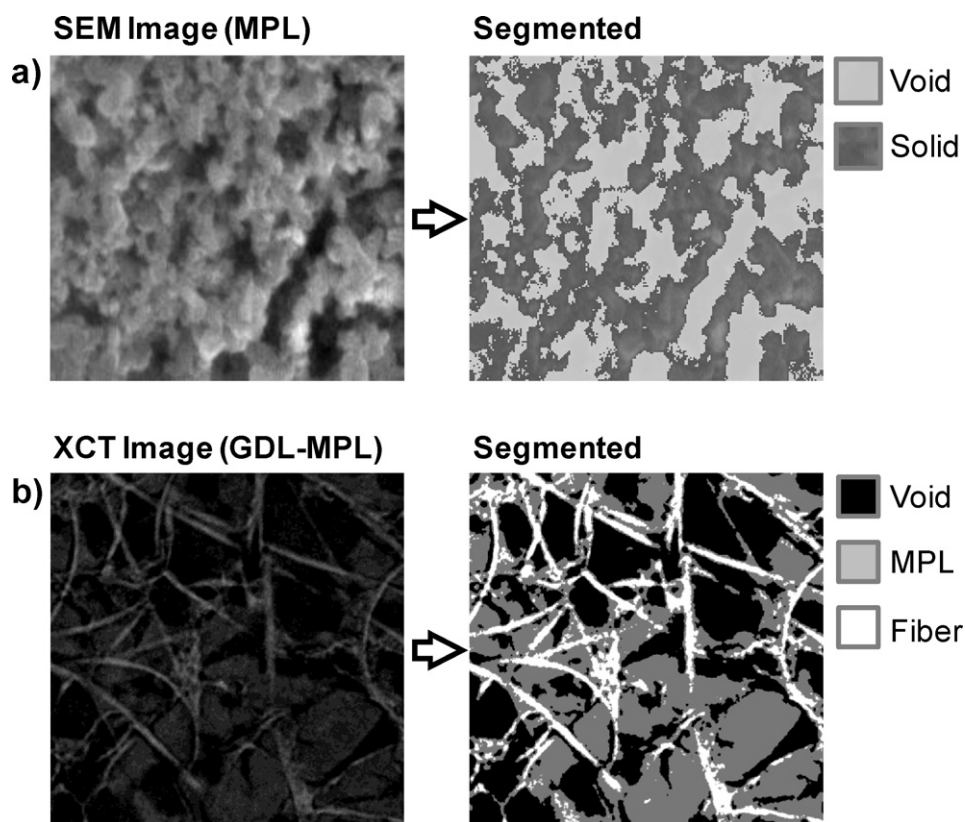

Fig. 2. Image post-processing: (a) segmentation of FIB–SEM images into void and solid using the ISODATA algorithm [34–38] and (b) segmentation of XCT images into void, MPL, and fiber phases using the EM/MPM/SA algorithm [41].
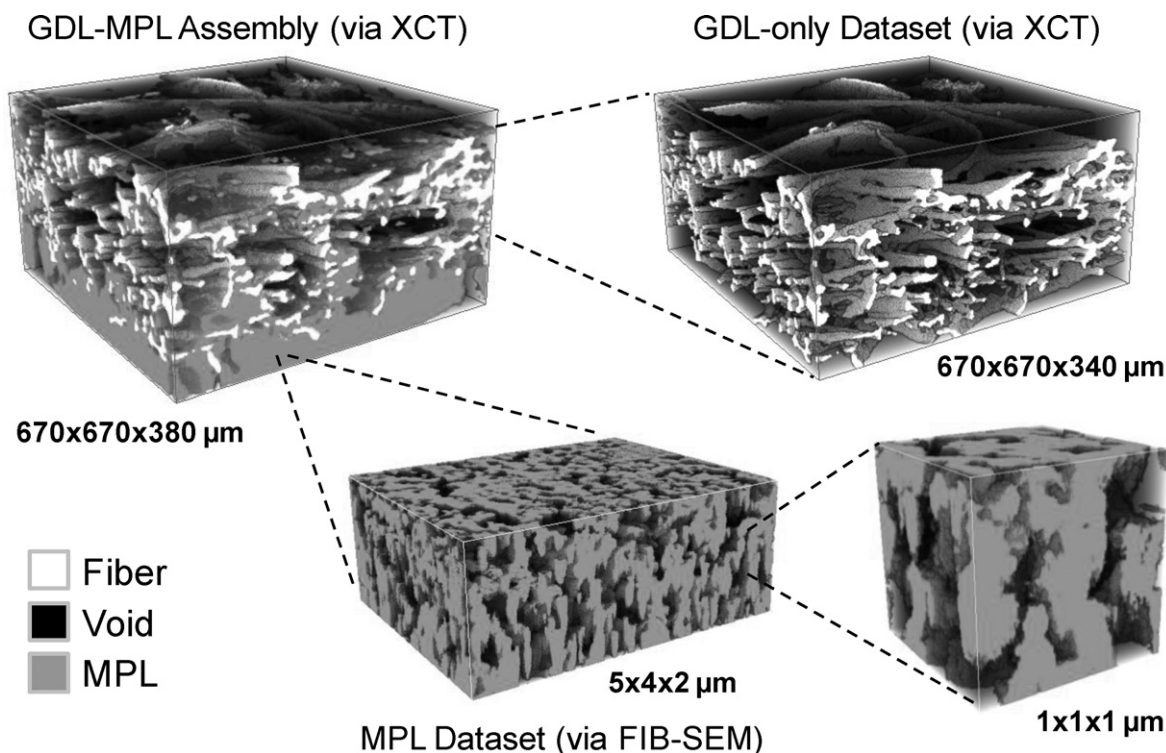
Fig. 3. 3-D reconstructions of the GDL–MPL assembly using XCT, the GDL-only dataset (top right), and the MPL dataset (bottom) captured using FIB–SEM.

floating in void space. Finally, the segmented dataset was coarsened by a factor of two in order to reduce the computation time required to run the structure analysis algorithms. The coarsening altered the global phase volume fractions by less than 1% and showed virtually no changes upon visual inspection. The final dataset with a resolution of 2.24 μm/voxel is shown in the top left of Fig. 3.

2.1.3. Capturing GDL-only dataset

Once the microstructure of the GDL–MPL assembly was captured, the GDL-only dataset (Fig. 3) was extracted from the XCT data by examining the through-plane phase volume fraction distribution of the GDL–MPL assembly shown in Fig. 4. The cut-off point for the GDL-only dataset was determined by examining the fiber phase distribution to find the first slice which contains at least 1% fiber phase (i.e., where the GDL region starts to appear). Based on the phase distribution, the fiber phase volume fraction was first found to be 1% in slice 20 as shown in Fig. 4. The slices beyond this point contain the fibrous GDL substrate and therefore can be assumed to contain the GDL dataset. The through-plane fiber phase distribution steadily increases in volume fraction through slices 20–40 and decreases in volume fraction through slices 150–170, with a plateau in the middle. The GDL-only dataset was created by removing the preceding 19 slices from the GDL–MPL assembly and converting any remaining MPL voxels to void voxels.

As seen in the XCT image (Fig. 4), there is no distinct interface between the GDL and MPL regions. Instead, the GDL|MPL interface is fairly thick, spanning well beyond slice 20 (for tens of microns) until approximately slice 55, where the fiber and MPL phase distributions intersect. Therefore, it is reasonable to assume that slice number 55 is an 'approximate' end point for the GDL|MPL interface. It is important to note that in this study, the GDL|MPL interface is considered as the boundary region that separates the *core* GDL and MPL regions, and is only identified herein to help capture the GDL-only dataset. Since the GDL|MPL interface contains a significant amount of fiber phase, slices 20–55 are not excluded from the GDL-only dataset. Therefore, the captured GDL-only dataset in
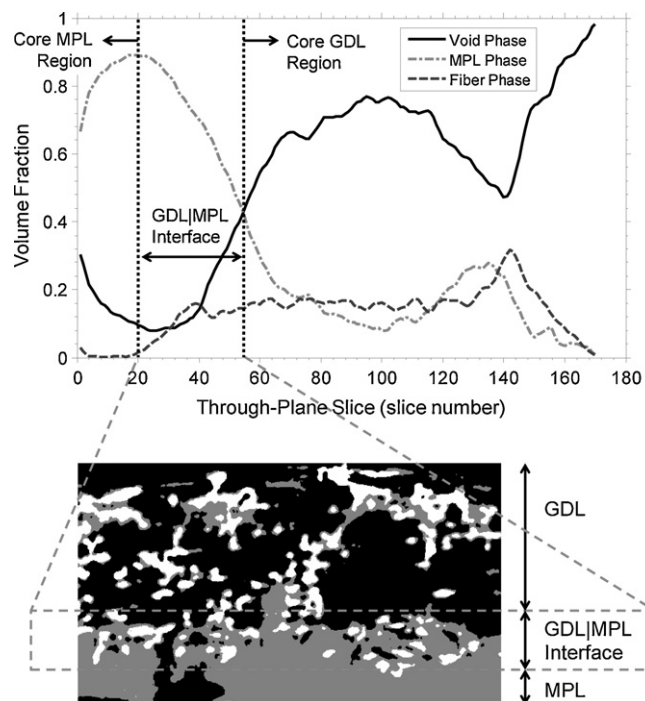

Fig. 4. Through-plane phase volume fraction distribution (top) and a segmented XCT image of the through-plane cross-section (bottom) of the GDL–MPL assembly, showing each region and the GDL|MPL interface. The cut-off point for the GDL-only dataset was determined by examining the distribution (top image) to find the first slice which contains at least 1% fiber phase (slice 20). The GDL-only dataset was then created by removing the first 19 slices and converting any remaining MPL voxels to void voxels.

this study comprises both the *core* GDL substrate and the fibrous portion of the GDL|MPL interfacial region.

2.2. Property (metric) evaluation of microstructure datasets

2.2.1. Quantification of structure-related properties

Once the 3-D reconstructions have been successfully generated, the microstructure analysis tools were applied to all three datasets (i.e., GDL-only, MPL-only and GDL–MPL assembly) to determine important measures of structure, including: the phase volume fractions (e.g., porosity), pore connectivity, tortuosity, structural diffusivity coefficient, and chord length distributions. A summary of the microstructure analysis tools is included below, and more detailed descriptions of these algorithms can be found in our previous publications [34,35].

Each phase volume fraction (e.g., porosity) was calculated by taking the ratio of the number of voxels of the given phase to the total number of voxels in the 3-D reconstruction [34,35]. For the pore phase, an important property of interest is the pore connectivity, which indicates the fraction of the pore volume that is available for transport in a given direction. This direction was specified using a pair of opposing external faces, which represent the entry and exit surfaces for transport through the reconstructed volume. As such, the image volume was first analyzed to identify the 3-D voxel network within the void phase which connects the entry and exit surfaces. The remaining portion of the void phase was deemed "unconnected" and therefore assumed unavailable for transport. The pore connectivity was then calculated as the ratio of the number of "connected" void voxels to the total number of void voxels [34,35].

In terms of tortuosity, a Dijkstra-based search algorithm was used to compute tortuous paths within the measured microstructure. In this approach, the measured 3-D structure dataset is transformed into a 2-D adjacency matrix, where each node represents a voxel (e.g., pore or solid in the case of the MPL), and each link represents a physical connection between the two voxel nodes [34,35]. Each link between any two pore voxels represents the Euclidean distance between the two. The search algorithm then finds the shortest possible path from a designated starting node on the entry surface to any end node on the exit surface. The tortuosity value for a given path is calculated by dividing the length of the tortuous path by the shortest distance between the entry and exit surfaces (i.e., the thickness of the volume). In this manner, a distribution of tortuosity may be achieved for the 3-D material structure by determining a pathway from every pore voxel on the entry surface. For complex materials like the DM, a tortuosity distribution provides much more insight into the tortuous nature than a single effective value [34,35].

The structural diffusivity coefficient, K_{SD}, is another key property of interest since it captures the unique diffusive resistance of a species in a given material structure. The value of K_{SD} can be used to estimate the effective diffusivity, D_{eff}, of a species:

$$D_{eff} = K_{SD} \cdot D_{i,j} \tag{1}$$

where $D_{i,j}$ is the bulk diffusivity of species i in species j. This characteristic K_{SD} value was determined using a 3-D diffusion model based on a finite volume approximation of the steady state Fickian diffusion model [34,35]. The model domain was represented by the voxelated material structure, where each void voxel serves as a finite volume available for diffusion with a net flux maintained at zero. A concentration gradient was induced between the entry and exit surfaces. The opposing lateral surfaces of the structure were subjected to periodic boundary conditions to prevent any net flux in the in-plane directions. The resulting estimate of net flux in the through-plane direction was used to calculate the value of K_{SD}. It should be noted that the K_{SD} value of the MPL determined

with this approach is expected to be slightly higher than the actual value, since transport in the MPL is partially governed by Knudsen diffusion [42,43].

To obtain information regarding the size distribution of the pores (i.e., void space), chord length distributions were determined for the 3-D microstructure datasets of the GDL-only and MPL-only regions. As compared to conventional techniques, the chord length approach can capture the rough/jagged morphology of the pores in fuel cell DM more accurately, since this approach (unlike traditional techniques) is not based on the assumption of idealized circular/spherical pore geometry. Here, a chord is defined as a line in a particular orientation which connects two phase boundaries within the microstructure while lying completely within the pore (void) phase [34]. The start and end points of a chord are located at the phase boundaries and form a pair of points that define the chord for a given orientation [34], where the length of a chord can be estimated by the Euclidean distance between the boundary pixel pair. This algorithm captures an orientation-specific chord length distribution by recording the length of all chords within the 3-D voxelated structure at the given orientation [34]. Chord length distributions can be determined for multiple orientations to identify the degree of anisotropy. In this study, only the three primary orthogonal orientations were considered for simplicity.

2.2.2. Estimation of transport properties via full morphology model

In addition to the structure-related metrics, key transport properties (including permeability and capillary pressure–saturation curves) of the MPL, GDL-only, and GDL–MPL assembly regions were determined from direct numerical simulations of the flow in the measured 3-D microstructure datasets. Permeability simulations were performed using the GeoDict software package. In these simulations, the permeability, k, of the porous structure was defined using Darcy's law:

$$v = -\frac{k}{\mu} \nabla P \tag{2}$$

where μ is the dynamic viscosity of the fluid [44]. In Darcy's law, the tensor k describes the proportionality constant between the average flow velocity, v, of a slow viscous flow through the porous medium and the applied pressure gradient, ∇P. In this sense, k does not depend on the fluid and is a pure geometric property measured in darcy (1 darcy = 10^{-12} m^2). The simulations were performed on the 3-D microstructure datasets to determine the value of v for a given ∇P. In the last few years, several studies have been published which describe how this flow problem can be numerically solved in complex geometries (such as in fuel cell DM) using the Lattice-Boltzmann approach [29] or Immersed Boundary Method [45]. Both methods are included in the GeoDict software package [46] and have been utilized in this study to compare the predicted permeability values for the tested microstructures.

To determine the water retention characteristics of the tested DM sample, we have focused on the evaluation of the primary drainage curves for the measured microstructures. The drainage process is closely related to quasi-static two-phase flow conditions, and can be simulated via a full pore morphology (FM) model [47–49]. In previous studies, the FM model has been applied successfully to various porous media, including soil samples, sintered glass, wovens, and non-wovens [45,48–50]. In the following paragraphs, we give a short overview of the FM model which was used in this study to determine the capillary pressure–saturation curves of the 3-D datasets. More detailed information regarding the FM model formulation can be found in our previous publications [48,49].

During the simulations of the quasi-static drainage process, one side of the porous medium is assumed to be connected to a wetting

Table 1
Key structure-related properties of the GDL-only, MPL-only, and GDL–MPL assembly datasets, predicted using sets of 300 random volumes. For the GDL-only and GDL–MPL assembly datasets, the random volumes have an in-plane window size of 50×50 pixels. For the MPL-only dataset [34], the random volumes have a window size of $100 \times 100 \times 100$ pixels ($\sim 1\,\mu m^3$).

	GDL-only dataset	MPL-only dataset	GDL–MPL assembly dataset	Units
Void volume fraction (porosity)	0.85 ± 0.03	0.42 ± 0.04	0.52 ± 0.07	Fraction
Fiber volume fraction	0.15 ± 0.03	N/A	0.13 ± 0.03	Fraction
Tortuosity	1.07 ± 0.02	1.33 ± 0.08	1.18 ± 0.03	Ratio
Structural diffusivity coefficient	0.45 ± 0.088	0.225 ± 0.045	0.229 ± 0.052	Fraction

phase (WP) reservoir, and the opposite end to a non-wetting phase (NWP) reservoir. Initially, the entire pore space is filled with the WP, which yields a zero capillary pressure condition. The pore space is then eroded by a spherical structuring element with radius, r. Using the Young–Laplace equation, the corresponding capillary pressure P_c is calculated as

$$P_c = \frac{2\gamma \, \cos\theta}{r} \qquad (3)$$

where γ is the surface tension between the NWP and WP, and θ is the contact angle between the NWP and solid. In the eroded pore space, all pores which have a continuous connection to the NWP reservoir are filled with the NWP, and the unconnected pores are removed from the eroded space. In the next step, the eroded and connected pore spaces are dilated by the same spherical structuring element, so that the dilated pore space corresponds to the volume which is only occupied by the NWP at the given value of P_c. This erosion–connection–dilation process is repeated with spherical elements of decreasing size (i.e., increasing P_c) until the entire pore space is filled with the NWP. At each step, the capillary pressure and corresponding saturation value are recorded and the local water distributions are captured for the 3-D datasets.

3. Results and discussion

3.1. Selection of small random volumes for metrics analysis

The microstructure analysis protocols described in Section 2.2.1 were applied to sets of small, randomly selected volumes from within the GDL-only and the GDL–MPL assembly datasets. The main goal behind the selection of small volumes was to enable execution of the microstructure analysis algorithms in a reasonable time frame, since the run time can scale rapidly with the size of the volume being processed. A similar analysis using a high number of randomly selected volumes was performed in our previous studies on the MPL microstructure (i.e., MPL-only dataset) [34,35], and the key results are summarized here to support the analysis of the MPL and GDL regions. In the case of the GDL-only and GDL–MPL assembly datasets, each randomly selected volume has an in-plane window size of 50×50 pixels ($\sim 110\,\mu m \times 110\,\mu m$). To preserve the dual-layer structure of the GDL–MPL assembly and the through-plane effects, each random window was selected such that it captures the entire thickness of the full datasets. As such, the volumes selected from the GDL-only and GDL–MPL assembly datasets have through-plane thicknesses of $\sim 340\,\mu m$ and $\sim 380\,\mu m$, respectively. Furthermore, the same in-plane window locations were used for both the GDL-only dataset and GDL–MPL assembly dataset to ensure that a direct structural comparison can be made between the datasets.

Three different groups of small volumes (i.e., 100, 200, and 300 random volumes) were evaluated to gauge the changes in the predicted values of the structure-related properties, including the phase volume fractions (void and fiber), tortuosity, and structural diffusivity coefficient. Very little variation (less than 3%) is observed between the property values predicted for the three groups of volumes, indicating that the measured microstructures

have been sufficiently sampled. To further evaluate the selection of smaller volumes, the void, MPL and fiber volume fractions were determined for the *full* MPL, GDL-only and GDL–MPL datasets (i.e., without using random smaller volumes). The predicted volume fractions for the full datasets were found to match the averages for the corresponding set of 300 random volumes to within less than 1% error. Table 1 shows the results of these properties for the 300 random volumes obtained from all three datasets.

3.2. Structure-related properties (metrics)

3.2.1. Porosity and pore connectivity

Table 1 shows the predicted porosity values for the GDL-only and the MPL-only datasets. It is important to note that the segmentation techniques used in this study yield an estimate of porosity based on automated segmentation, such that they do not target a specific porosity value. The estimated porosity of the MPL (~ 0.42) agrees well with reported values in literature (e.g., 0.4–0.6) [29,39,40], and the GDL-only porosity is found to be fairly close to the porosity of 0.88 reported by the manufacturer for SIGRACET® SGL 10BA (with no MPL applied). The results also show that the pore connectivity of the full GDL-only dataset is around $\sim 99\%$, indicating that almost the entire void space is a single connected network with few isolated voids/pores. This can be attributed to the fact that the GDL is constructed as a matting of nonwoven carbon fibers, which yields a highly connected network of pore space.

3.2.2. Tortuosity distribution

Fig. 5 shows the computed tortuosity values based on the analysis of all 300 random volumes selected from the MPL, GDL-only, and GDL–MPL assembly datasets. The majority of the pathways identified in the GDL-only dataset (Fig. 5a) are found to be relatively straight with an effective (average) tortuosity of 1.07 ± 0.02. This can be attributed to the high porosity and relatively open pore structure of the GDL region. In our previous study [34], the tortuosity analysis was performed on the MPL-only dataset and yielded an average tortuosity value of 1.33 (Fig. 5b), which is higher than the tortuosity of the GDL-only dataset. This average tortuosity value was taken as an "effective length" of travel through the porous structure of the MPL, and was applied here to each MPL voxel in the GDL–MPL assembly to determine the tortuosity distribution of GDL–MPL assembly.

Fig. 5c shows the computed tortuosity distribution for the GDL–MPL assembly. The addition of the MPL in the GDL–MPL assembly appears to induce a tortuous barrier which increases the tortuosity to an effective value of 1.18 ± 0.03 ($\sim 10\%$ increase from the GDL-only dataset). The tortuosity range for the GDL–MPL assembly still spans down to low values (around 1.05) due to the presence of relatively large cracks and holes which penetrate through the entire thickness of the MPL region. Such cracks in the MPL region were observed in the previous studies by Fishman and Bazylak [17] and Hizir et al. [51]. The calculated tortuous pathways tend to migrate toward these large cracks and holes, which are naturally less resistive. If these cracks/holes did not exist, one would
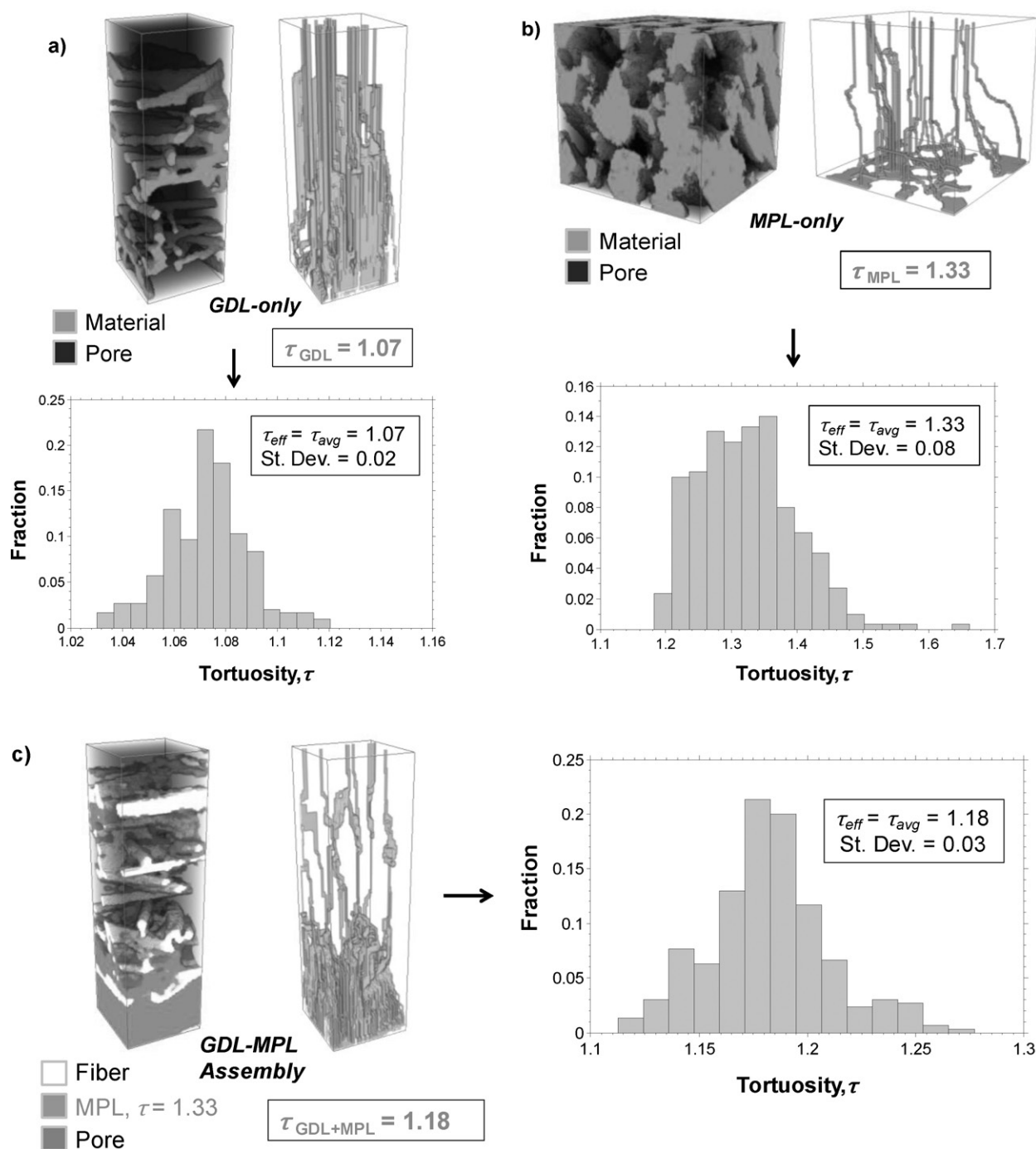
Fig. 5. Tortuosity distributions for the (a) GDL-only, (b) MPL-only [34], and (c) GDL–MPL assembly datasets. A random volume is shown for each dataset for demonstration purposes. Each distribution is based on 300 random volumes selected from the full dataset.

expect that the addition of the MPL would result in a more drastic increase in tortuosity for the GDL–MPL assembly.

3.2.3. Structural diffusivity coefficient

The structural diffusivity coefficient (K_{SD}) analysis was performed in the through-plane direction on the 300 randomly selected volumes from the GDL-only dataset. Fig. 6a shows the distribution of K_{SD} for the GDL-only dataset, which has an average K_{SD} value of 0.45. Similarly, the diffusion model was applied to the MPL-only dataset in our previous study [34], and an average K_{SD} value of 0.225 (Fig. 6b) was determined for the MPL-only dataset. When compared, the smaller K_{SD} value of the MPL indicates the existence of a higher diffusion resistance in the MPL

region, which can be directly attributed to the much lower porosity and relatively more tortuous nature of the MPL structure. To further analyze the GDL–MPL assembly, the predetermined K_{SD} value of 0.225 was applied to each MPL voxel in the 300 random volumes of the GDL–MPL assembly dataset. Fig. 6c shows the structural diffusivity coefficient distribution for the GDL–MPL assembly dataset, which has an average K_{SD} value of 0.229. The addition of the MPL appears to cause a drop in K_{SD} of almost 50% for the GDL–MPL assembly when compared to the GDL-only dataset. Furthermore, the K_{SD} value determined for the GDL–MPL assembly is observed to be nearly equivalent to that of the MPL dataset. These findings suggest that the fine and tortuous microstructure of the MPL region creates a significant diffusive barrier, which dominates
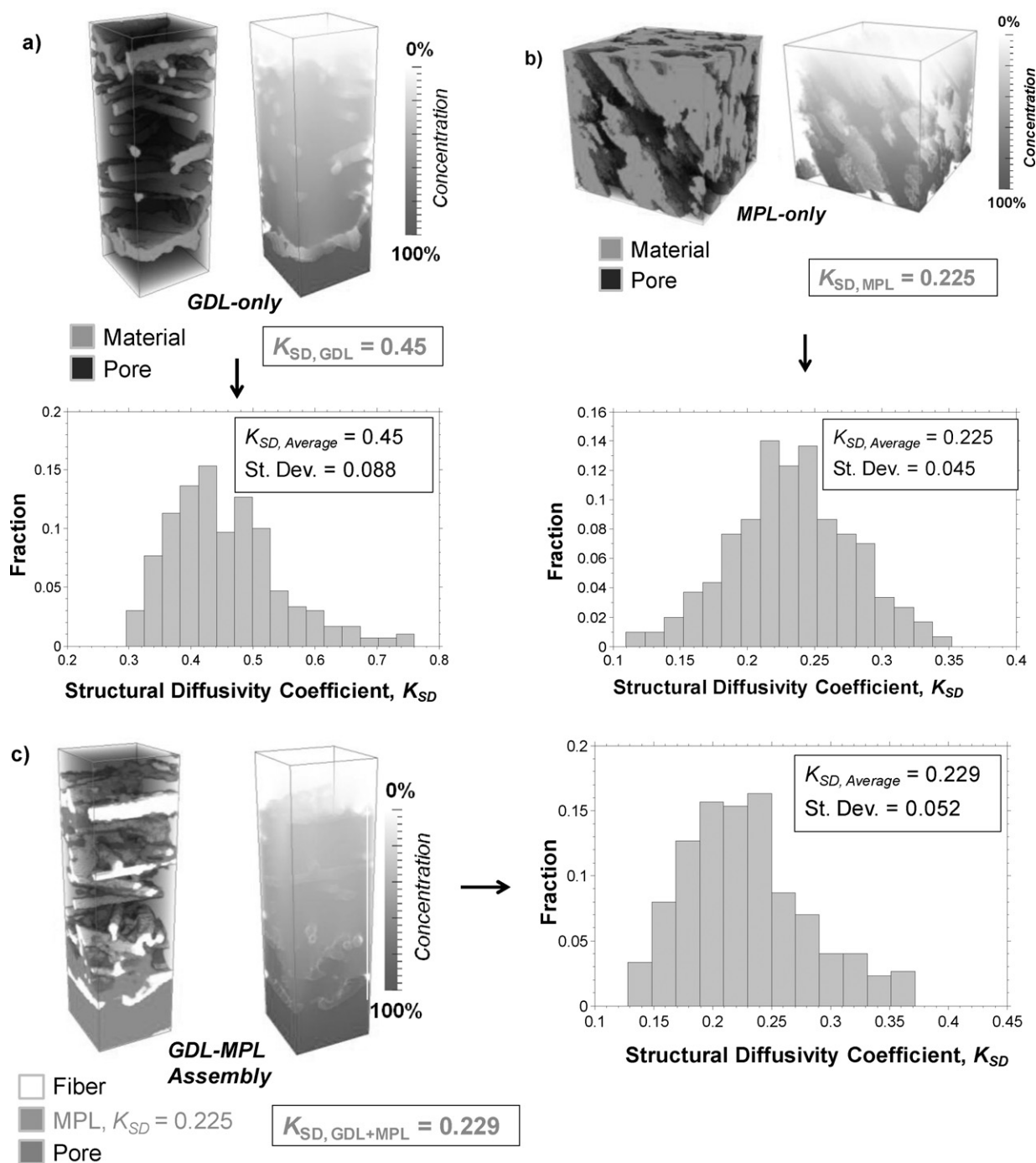
Fig. 6. Structural diffusivity coefficient distributions for (a) GDL-only, (b) MPL-only [34], and (c) GDL–MPL assembly datasets. A random volume is shown for each dataset for demonstration purposes. Each distribution is based on 300 random volumes selected from the full dataset.

the overall diffusive transport behavior of the GDL–MPL assembly.

3.2.4. Chord length (pore size) distribution

Chord length distributions were determined in the three primary orthogonal directions (i.e., x, y, and z) for the void phase of the full GDL-only and MPL datasets, and are shown in Fig. 7. Fig. 7a indicates that the voids (pores) in the GDL-only dataset are generally below 100 microns in dimension, with an average chord length (mean pore size) of 85 μm. Similarly, the voids in the MPL are observed to be primarily below 500 nm in size with a mean pore size of 320 nm (Fig. 7b).

Compared to the GDL-only region, the pore sizes of the MPL-only dataset are found to be approximately three orders of magnitude smaller. These results support the existence of a high diffusive resistance in the MPL, suggesting the dominance of the MPL region on the overall diffusion characteristics of the GDL–MPL assembly. The chord length distributions also indicate the existence of some degree of anisotropy in the MPL-only and GDL-only datasets. However, the extent of anisotropy is observed to be more significant in the GDL-only dataset, particularly with regards to in-plane (x and y) versus through-plane (z) directions. This is possibly due to the fact that the GDL is constructed from fibers which primarily lay flat in the x–y plane.
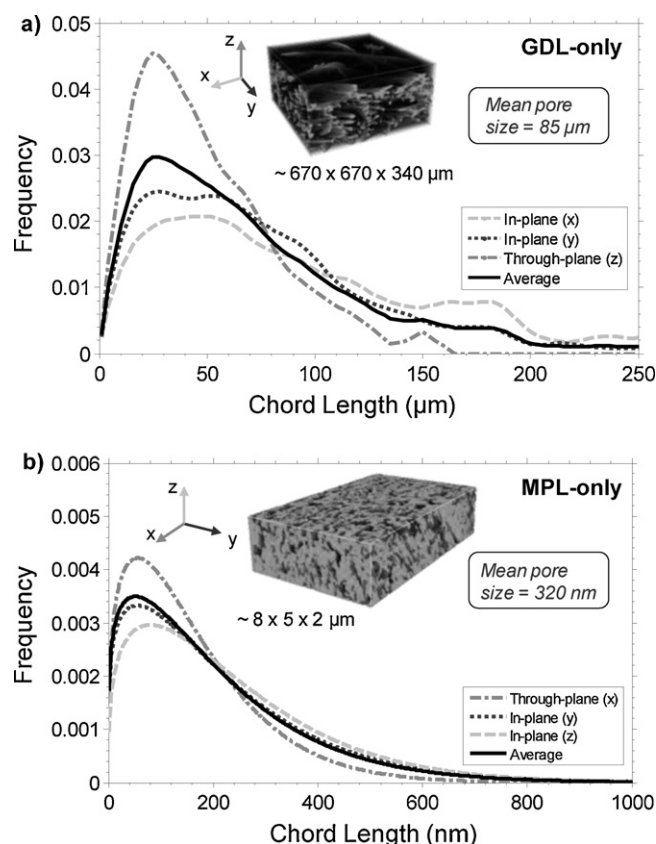
Fig. 7. Chord length distributions for the pore (void) phase of (a) the full GDL-only dataset and (b) the full MPL-only dataset [34]. Distributions in the three primary orthogonal directions and the average of the three distributions are included for each dataset.

3.3. Flow properties – permeability and capillary pressure

The measured datasets were analyzed using the GeoDict software and the FM model to determine the effective permeabilities and capillary pressure–saturation curves for these regions. The simulations were performed on the *full* datasets in both the in-plane and through-plane direction to determine the level of anisotropy in these transport properties.

3.3.1. Through- and in-plane permeability

The through-plane and in-plane permeabilities of the MPL-only dataset were found to be smaller than $2 \times 10^{-16}\,\mathrm{m}^2$, which is below the convergence limit of the employed solver. This value serves as an upper limit for the permeability of the MPL-only dataset and also agrees well with the results reported by Ostadi et al. [29], which are on the order of $10^{-16}\,\mathrm{m}^2$ or below. Furthermore, this upper limit is approximately six orders of magnitude smaller than the permeability values predicted for the GDL-only dataset. Ostadi et al. [29] also noted a similar difference in magnitude between the permeability values of their MPL and GDL datasets.

For the GDL-only dataset, the calculated permeability for the in-plane direction ($1.22 \times 10^{-10}\,\mathrm{m}^2$) is found to be ~2.2 times higher than the through-plane permeability ($0.55 \times 10^{-10}\,\mathrm{m}^2$), indicating the existence of more favorable flow in the in-plane direction. When compared to the permeability measurements of 0.33×10^{-10} and $0.18 \times 10^{-10}\,\mathrm{m}^2$ reported by Ihonen et al. [52] for SIGRACET® SGL 10BA, the results from our simulation are ~3–4 times higher. This discrepancy may be partially related to the fact that our GDL-only dataset was obtained by extraction

from XCT data of a sample of SIGRACET® SGL 10BC (coated with MPL), rather than by directly quantifying a sample of SGL 10BA (which has no MPL); therefore, the data may not be directly comparable.

3.3.2. Capillary pressure–saturation curves

The capillary pressure–saturation curves were determined using the FM model in two ways: (i) by performing a numerical simulation of primary drainage and (ii) by assuming arbitrarily mobile fluids [49]. In the primary drainage simulation, the quasi-static saturation states for the WP (air) and NWP (water) distributions were obtained over the range of capillary pressures. An average contact angle of 120° was assumed for the datasets based on the direct comparison of the experimental observations reported in Benziger et al. [53] and the FM model predictions [49]. The entire pore space was initially filled with the WP, and the overall modeling domain was connected to a WP and NWP reservoir at opposite ends, while the lateral faces were closed for intrusion of water or air. The capillary pressure was then increased in a step-wise fashion starting from zero, and the imbibition of the NWP into the 3-D structure was simulated until full saturation was reached. For the alternate simulation (arbitrarily mobile fluids), the FM algorithm was applied by neglecting the connectivity of the pores to the NWP reservoir [49]. In addition, the pore space was considered as a bundle of capillaries whose connectivity is neglected. Therefore, the capillary pressure curves generated in this manner physically correspond to saturation levels due to arbitrary motion of the wetting and non-wetting fluids, and can be considered as a lower bound of the capillary pressure–saturation curve [49].

Fig. 8 shows the capillary pressure–saturation curves obtained from the FM model for the *full* GDL-only, MPL-only, and GDL–MPL assembly datasets. The predicted capillary pressure–saturation curves show reasonably good agreement with the experimental curves obtained by Gostick et al. [54] for SGL 10BA in terms of the trend and magnitude of capillary pressure. For the GDL-only dataset, the results for in-plane drainage show slightly higher capillary pressures at lower saturation values (0–0.3) as compared to the through-plane direction, suggesting more favorable capillary transport in the through-plane direction. This prediction agrees with the larger pore sizes seen in the chord length distributions of the GDL-only dataset for the orientations normal to the through-plane direction (i.e., x and y). Additionally, both drainage curves are observed to be close to the lower bound obtained by assuming arbitrarily mobile fluids, which indicates that the pore space of the GDL is highly connected and agrees with the high connectivity values predicted for the GDL-only dataset.

The capillary pressure–saturation curves for the MPL-only dataset (shown in Fig. 8b) are significantly different from the GDL-only dataset curves, primarily due to the large difference in pore sizes between the GDL-only and MPL-only dataset. In particular, the capillary pressures observed in the MPL dataset are roughly three to four orders of magnitude higher than that of the GDL-only dataset. Therefore, it is very unlikely that liquid water will flow or intrude into the fine pore structure of the MPL under typical PEFC operation, unless large elongated cracks exist in the MPL structure. When the through-plane and in-plane drainage curves are compared, both curves exhibit similar behavior, but show capillary pressures ~25–50% higher than the lower bound obtained *via* simulation of arbitrarily mobile fluids. This can be attributed to the rougher surface and more convoluted nature of the internal structure of the MPL.

For the analysis of the GDL–MPL assembly, all MPL voxels were assumed to be impermeable to liquid water (i.e., solid) due
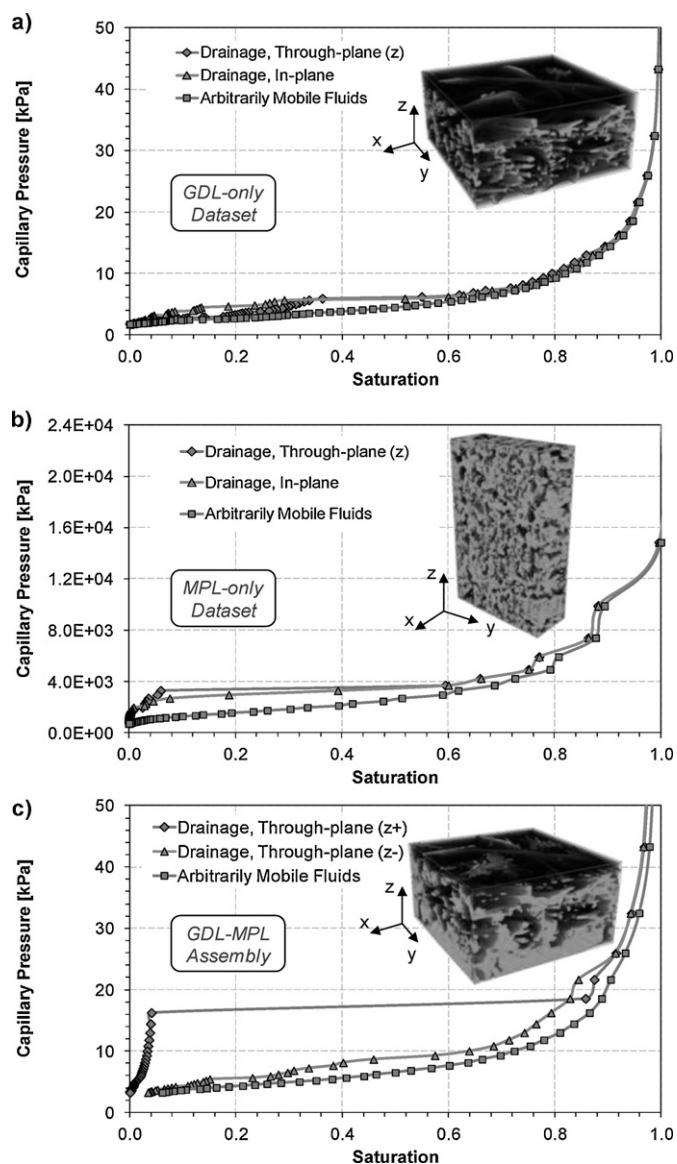
Fig. 8. Capillary pressure–saturation curves determined from the FM model for the (a) GDL-only, (b) MPL-only, and (c) GDL–MPL assembly datasets.

levels can be easily reached at much lower capillary pressures due to the larger pores of the GDL region. Upon reaching the threshold pressure for the z+ direction around 18 kPa, the GDL–MPL assembly becomes saturated rapidly, and the remainder of the capillary pressure–saturation curve shows a trend similar to the other curves. The predicted spike in saturation over a small increase in capillary pressure has also been observed in Ref. [54].

3.4. Visualization of water imbibition in measured microstructures

Fig. 9a shows the visualization sequence of the water distribution in the GDL region as the capillary pressure increases until the bubble point for the GDL-only dataset. Here, the bubble point is defined as the pressure at which water first reaches the top surface of the GDL region. As the capillary pressure approaches the bubble point ($P_c \sim 6$ kPa), the GDL-only dataset exhibits a rapid increase in saturation (from $\sim$0.35 to 0.55) for only a small increase in capillary pressure, as shown in Fig. 8a. This can be attributed to the fact that once a threshold capillary pressure is reached which is high enough to break through the majority of pores at the GDL entry surface, it is very likely that the remaining thickness of the GDL can be easily imbibed due to the relatively open pore structure of the fibrous GDL. Fig. 9a also supports this observation, showing a sudden water coverage of the GDL when the capillary pressure is increased from 5.91 kPa to 6.19 kPa.

Similar visualization sequences are shown in Fig. 9b and c for the MPL-only and GDL–MPL assembly datasets, respectively. As compared to the GDL-only dataset, a more steady increase in saturation level is seen as the bubble point is approached in the MPL-only dataset (Figs. 8b and 9b). This can be attributed to the denser and more complex structure of the MPL, which is composed of a network of pores and restrictive throat connections that is fairly long in the through-plane direction (relative to pore size). When compared with the GDL-only data, significantly higher pressure is required to infiltrate the MPL substrate with water due to the high breakthrough resistance of the much smaller pores.

The visualization sequence shown in Fig. 9c for the GDL–MPL assembly is similar to that of the GDL-only dataset, in which a large increase in saturation is observed over only a small increase in capillary pressure as the bubble point is approached. However, this effect is much more dramatic for the GDL–MPL assembly in the z+ direction, where the saturation level jumps from approximately 0.05–0.85 (Fig. 8c). Upon reaching a certain pressure that is high enough for water to penetrate through the MPL region, the large pores of the remaining GDL region are easily infiltrated due to the fact that the pore structure of the GDL is much coarser, with pore sizes that are quite large relative to the overall thickness of the GDL–MPL assembly. These observations can be attributed to the fine structure of the MPL, which serves as a liquid water barrier with high capillary resistance; therefore fairly high capillary pressures are required for water to penetrate through the MPL region. Consequently, liquid water will likely penetrate only through the larger holes and cracks within the MPL, where the resistance is low (Fig. 9c). In the case of a crack-free MPL, it would be very challenging for liquid water to permeate into the MPL and reach the GDL region due to the high resistance. Therefore, it is reasonable to expect that water transport in a crack-free MPL will be more likely dominated by gas phase diffusion. These observations suggest that the presence of cracks and larger holes in the MPL region may be important features to facilitate the transport of liquid water from the catalyst layer through the cathode DM.
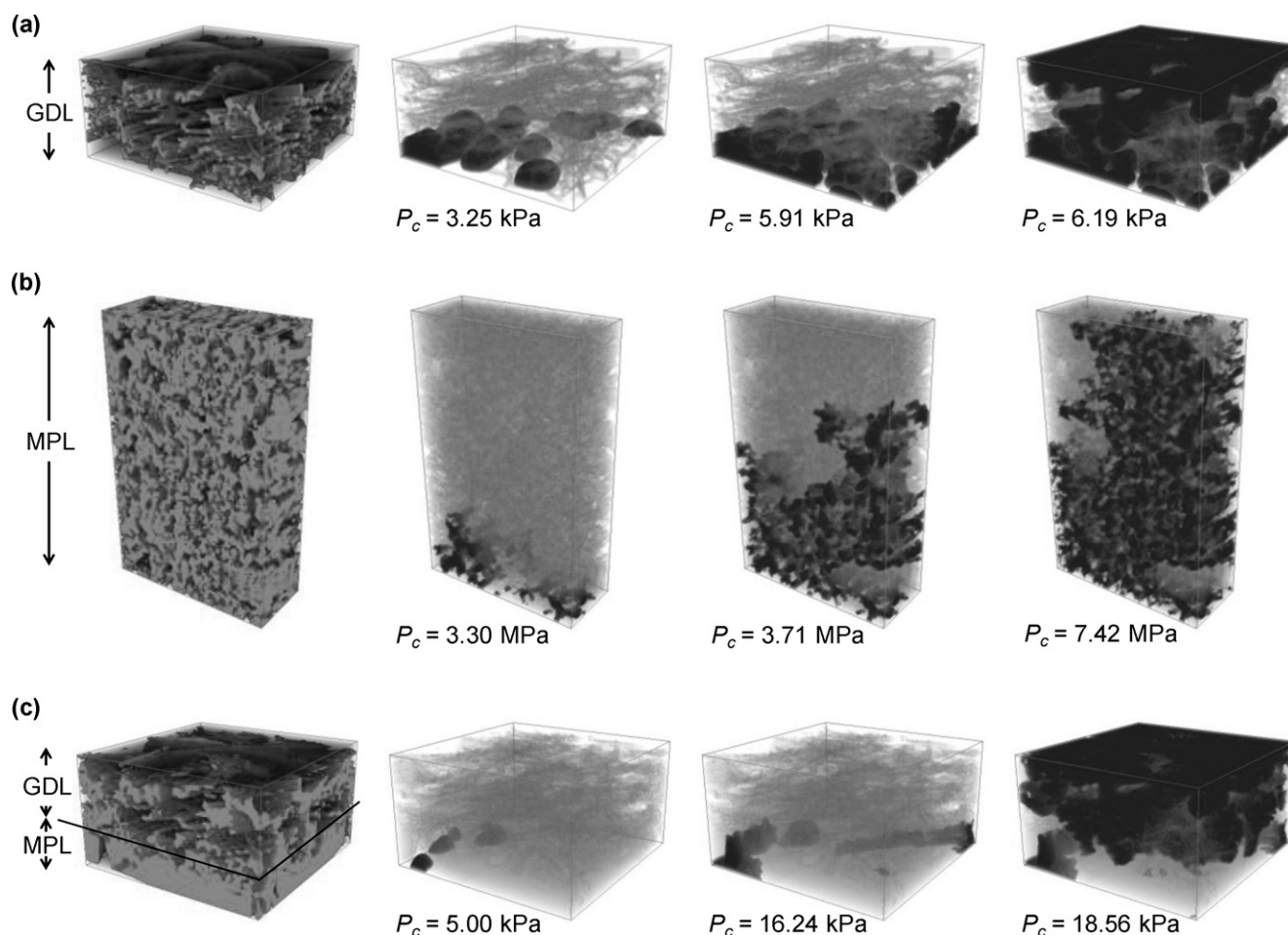
to the high capillary pressures observed in the fine structure of the MPL dataset (Fig. 8b). Since such high capillary pressures are unrealistic during PEFC operation, liquid water can only penetrate into the MPL through the larger holes and cracks within the MPL structure. For this reason, a GDL–MPL assembly dataset that has *cracks* in the MPL was selected to simulate the imbibition of liquid water. Accordingly, the drainage simulations for the GDL–MPL assembly were performed for two main directions (z+ and z−). Simulation for the z+ direction exhibits the condition of water penetrating or entering through the MPL side of the GDL–MPL region, whereas simulation in the z− direction considers the water first entering from the GDL side of the GDL–MPL assembly. As shown in Fig. 8c, the addition of the MPL in the GDL–MPL assembly results in a significant change in the capillary pressure–saturation curve results for the z+ direction. The curve spikes to relatively high capillary pressures at low saturation values (0–0.05) until a driving pressure is reached that is high enough to break through the small holes and cracks in the MPL region. This effect is not seen for drainage in the reverse z− direction (i.e., assuming water is first entering from the GDL side), because similar saturation

Fig. 9. Visualization sequence of the water distribution with respect to capillary pressure, P_c, for: (a) GDL-only, (b) MPL-only, and (c) GDL–MPL assembly datasets.

4. Conclusions

In this work, the microstructure of a dual-layer PEFC DM was quantified using both FIB–SEM and XCT to capture the fine and coarser structures of the MPL and GDL regions, respectively. Using the 3-D microstructure data, the MPL-only region, GDL-only region, and GDL–MPL assembly were analyzed at the pore scale to quantify the contribution of the MPL and GDL regions on the overall transport behavior of the GDL–MPL assembly.

The results indicate that the structure of the MPL has a significant impact on the transport properties of the GDL–MPL assembly. When the GDL-only dataset is compared with the GDL–MPL assembly, the addition of the MPL is found to cause an increase in tortuosity of ∼10%, and a decrease of nearly 50% in the structural diffusivity coefficient for the overall GDL–MPL assembly. Furthermore, the permeability of the MPL-only dataset is found to be six orders of magnitude smaller than the GDL-only dataset. This large difference can be attributed to the lower porosity, much smaller pore size, and more convoluted morphology of the MPL region, which creates a tortuous barrier of fine structure with high diffusive and pore entry resistance. Furthermore, fairly high capillary pressures are required for water to penetrate through the MPL, whereas the large pores of the GDL region are found to be easily infiltrated even at low capillary pressures. Simulation results also indicate that the presence of cracks and larger holes in the MPL region may aid in the removal of liquid water from the catalyst layer through the cathode DM, which can alleviate the flooding effects at the catalyst layer.

Acknowledgments

References

[1] R. Borup, J. Meyers, B. Pivovar, S. Kim, R. Mukundan, N. Garland, D. Myers, M. Wilson, F. Garzon, D. Wood, P. Zelenay, K. More, k. Stroh, T. Zawodzinski, X. Boncella, J. McGrath, M. Inaba, K. Miyatake, M. Hori, M. Ota, Z. Ogumi, S. Miyata, A. Nishikata, Z. Siroma, Y. Uchimoto, K. Yasuda, K. Kimijima, N. Iwashita, Chemical Review 107 (2007) 3904.
[2] N. Yousfi-Steiner, Ph Mocoteguy, D. Candusso, D. Hissel, A. Hernandez, A. Aslanides, Journal of Power Sources 183 (2008) 260.
[3] T. Swamy, E.C. Kumbur, M.M. Mench, Journal of The Electrochemical Society 157 (2010) B77.
[4] H. Bajpai, M. Khandelwal, E.C. Kumbur, M.M. Mench, Journal of Power Sources 195 (2010) 4196.
[5] M.M. Mench, Fuel Cell Engines, John Wiley & Sons, Hoboken, New Jersey, 2008.
[6] M.V. Williams, E. Begg, L. Bonville, H.R. Kunz, J.M. Fenton, Journal of The Electrochemical Society 151 (2004) 1173.
[7] M. Manahan, M.C. Hatzell Jr., E.C. Kumbur, M.M. Mench, Journal of Power Sources 196 (2011) 5573.

[8] Y.W. Chen-Yang, T.F. Hung, J. Huang, F.L. Yang, Journal of Power Sources 173 (2007) 183.
[9] T. Swamy, E.C. Kumbur, M.M. Mench, Electrochimica Acta 56 (2010) 3060.
[10] J.-H. Jang, W.-M. Yan, C.-C. Shih, Journal of Power Sources 161 (2006) 323.
[11] R.P. Ramasamy, E.C. Kumbur, M.M. Mench, W. Liu, D. Moore, M. Murthy, International Journal of Hydrogen Energy 33 (2008) 3351.
[12] K. Jiao, X. Li, Progress in Energy and Combustion Science 37 (2011) 221.
[13] E.C. Kumbur, K.V. Sharp, M.M. Mench, Journal of Power Sources 176 (2008) 191.
[14] J.T. Gostick, M.A. Ioannidis, M.W. Fowler, M.D. Pritzker, Journal of Power Sources 194 (2009) 433.
[15] E.C. Kumbur, K.V. Sharp, M.M. Mench, Journal of The Electrochemical Society 154 (12) (2007) B1295.
[16] J.D. Fairweather, P. Cheung, J. St-Pierre, D.T. Schwartz, Electrochemistry Communications 9 (2007) 2340.
[17] Z. Fishman, A. Bazylak, Journal of The Electrochemical Society 158 (8) (2011) B846.
[18] C. Siegel, Energy 33 (2008) 1331.
[19] N. Djilali, Energy 32 (2007) 269.
[20] E.C. Kumbur, K. Sharp, M.M. Mench, Journal of Power Sources 168 (2007) 156.
[21] K. Gallagher, R. Darling, T. Patterson, M. Perry, Journal of The Electrochemical Society 155 (2008) B1225.
[22] T.V. Nguyen, G. Lin, H. Ohn, X. Wang, Electrochemical and Solid-State Letters 11 (2008) B127.
[23] J.S. Preston, R.S. Fu, U. Pasaogullari, D.S. Hussey, D.L. Jacobson, Journal of The Electrochemical Society 158 (2) (2011) B239.
[24] K. Lee, J.H. Nam, C. Kim, Journal of Power Sources 195 (2010) 130.
[25] R. Wu, X. Zhu, Q. Liao, H. Wang, Y. Ding, J. Li, D. Ye, International Journal of Hydrogen Energy 35 (2010) 9134.
[26] J. Hinebaugh, Z. Fishman, A. Bazylak, Journal of The Electrochemical Society 157 (11) (2010) B1651.
[27] O.C.K. Aidun, J.R. Clausen, Annual Review of Fluid Mechanics 42 (2010) 439.
[28] T. Koido, T. Furusawa, K. Moriyama, Journal of Power Sources 175 (2008) 127.
[29] H. Ostadi, P. Rama, Y. Liu, R. Chen, X.X. Zhang, K. Jiang, Journal of Membrane Science 351 (2010) 69.
[30] B. Mondal, K. Jiao, X. Li, International Journal of Energy Research 35 (11) (2011) 1200.
[31] J.W. Park, K. Jiao, X. Li, Applied Energy 87 (2010) 2180.
[32] W.K. Epting, J. Gelb, S. Litster, Advanced Functional Materials 22 (2012) 555.
[33] H. Iwai, N. Shikazono, T. Matsui, H. Teshima, M. Kishimoto, R. Kishida, D. Hayashi, K. Matsuzaki, D. Kanno, M. Saito, H. Muroyama, K. Eguchi, N. Kasagi, H. Yoshida, Journal of Power Sources 195 (2010) 955.
[34] A. Cecen, E.A. Wargo, A.C. Hanna, D.M. Turner, S.R. Kalidindi, E.C. Kumbur, Journal of The Electrochemical Society 159 (3) (2012) B299.
[35] E.A. Wargo, A.C. Hanna, A. Cecen, S.R. Kalidindi, E.C. Kumbur, Journal of Power Sources 197 (2012) 168.
[36] G.H. Ball, D.J. Hall, Isodata, a novel method of data analysis and pattern classification, Technical Report AD 699616, Stanford Research Institute, Menlo Park, CA, 1965.
[37] T.W. Ridler, S. Calvard, IEEE Transactions: Systems, Man, and Cybernetics, SMC-8 (1978) 630.
[38] D. Ramachandram, Automatic thresholding, MATLAB Central File Exchange, http://www.mathworks.com/matlabcentral/fileexchange/3195 (31 Mar 2003).
[39] J. Becker, C. Wieser, S. Fell, K. Steiner, International Journal of Heat and Mass Transfer 54 (2011) 1360.
[40] K.T. Cho, M.M. Mench, Journal of Power Sources 195 (2010) 6748.
[41] J.P. Simmons, P. Chuang, M. Comer, J.E. Spowart, M.D. Uchic, M. De Graef, Modelling Simulation in Materials Science and Engineering 17 (2009) 025002.
[42] L.M. Pant, S.K. Mitra, M. Secanell, Journal of Power Sources 206 (2012) 153.
[43] A. Berson, H.W. Choi, J.G. Pharoah, Physical Review E 83 (2011) 026310.
[44] J. Bear, Dynamics of Fluids in Porous Media, 1st ed., Dover Publications Inc., New York, USA, 1972.
[45] J. Becker, V. Schulz, A. Wiegmann, Journal of Fuel Cell Science and Technology 5 (2008) 21006.
[46] GeoDict, Math2Market, Kaiserslautern, Germany.
[47] M. Hilpert, C.T. Miller, Advances in Water Resources 24 (2001) 243.
[48] H.-J. Vogel, J. Tolke, V.P. Schulz, M. Krafczyk, K. Roth, Vadose Zone Journal 4 (2005) 380.
[49] V.P. Schulz, J. Becker, A. Wiegmann, P.P. Mukherjee, C.-Y. Wang, Journal of The Electrochemical Society 154 (4) (2007) B419.
[50] V.P. Schulz, PhD Thesis, Universität Heidelberg, Germany, 2003.
[51] F.E. Hizir, S.O. Ural, E.C. Kumbur, M.M. Mench, Journal of Power Sources 195 (2010) 3463.
[52] J. Ihonen, M. Mikkola, G. Lindbergh, Journal of The Electrochemical Society 151 (8) (2004) A1152.
[53] J. Benziger, J. Nehlsen, D. Blackwell, T. Brennan, J. Itescu, Journal of Membrane Science 261 (2005) 98.
[54] J.T. Gostick, M.A. Ioannidis, M.W. Fowler, M.D. Pritzker, Electrochemistry Communications 11 (2009) 576.